ROYAL SOCIETY
OF CHEMISTRY

Check for updates

Continuous pore size gradient enhances zonal-specific differentiation of stem cells in an osteochondral scaffold

Gioacchino Conoscenti,†[ab] Kyra W. Y. Smith, [iD] †[cd] Alessandro Pirosa,‡[b] Francesco Carfì Pavia,[a] Emily Y. Zhang, [iD] [c] Vincenzo La Carrubba,[a] Valerio Brucato,[a] Rocky S. Tuan [iD] §[b] and Riccardo Gottardi [iD] ¶*[bcde]

Cartilage and bone in articular joints are intimately linked within the osteochondral (OC) unit. Scaffold-based regenerative approaches in the joint often target both cartilage and the subchondral bone, taking advantage of the endogenous bone marrow stem cells made available by breaching the OC junction. However, the production of scaffolds for OC regeneration is challenging, as scaffolds must provide mechanical strength while also mimicking the local cartilage and bone microenvironments. To create an osteochondral scaffold, we used Thermally Induced Phase Separation (TIPS) that allows us to create a wide range of morphologies in terms of pore size and distribution by tuning thermal history. We created a poly-L-lactic acid (PLLA) scaffold with a continuous pore size gradient from 70 μm diameter on the cartilage repair side to over 200 μm diameter on the bone repair side. We hypothesized that the smaller pore size will support chondrogenesis while the larger pore size will induce an osteogenic phenotype. This hypothesis was confirmed using an innovative biphasic bioreactor capable of providing distinct and separate signaling cues for cartilage and bone differentiation, while allowing communication across the osteochondral junction, similar to the *in vivo* environment. Our findings suggested that the PLLA continuous pore-gradient structure may offer a clinically translatable solution to osteochondral defect repair by supporting zone-specific differentiation.

Introduction

Osteochondral defects affect over 60% of patients that undergo knee surgery and present a major health and mobility concern.[1] Such osteochondral lesions are characterized by damage to both articular cartilage and the underlying subchondral bone, which can occur from either acute trauma, underlying bone disorders, or long-term degeneration, such as osteoarthritis.[2] Current standards of care do not restore the native tissue.[3] For instance, microfracture leads to fibrocartilage formation,[4] and allografts are subject to low donor availability and insufficient tissue size.[5] Thus, tissue engineering represents an exciting alternative, but a common setback is the difficulty of creating engineered tissues representative of native tissue.[6]

Articular cartilage is a highly organized tissue with complex architecture that bestows compression resistance, high tensile strength, and frictionless joint movement.[7] This complexity, however, is rarely matched by engineered cartilage. Furthermore, engineered cartilage, depending on the cell and processes used, may calcify or present a more fibrocartilaginous phenotype.[6,8] The addition of growth factors such as transforming growth factor-β3 (TGF-β3), bone morphogenetic proteins (BMP), and fibroblast growth factor-2 (FGF-2), can help guide engineered cartilage formation. Sarsenova *et al.* showed that delivering TGF-β3 and BMP-4 alongside stem cells drastically improved osteochondral defect repair in a rabbit model compared to stem cells alone.[9] Additionally, delivery of recombinant human FGF-2, clinically known as Sprifermin,[10] is in phase II clinical trials showing a reduction of cartilage loss.[11] Despite promise, there are very few growth factor delivery systems available on the market,[12] and none for repair or regeneration of osteochondral defects.[13] Apart from regulatory challenges,[14] the translation of growth factor delivery to the

ᵃDepartment of Civil, Environmental, Aerospace, Materials Engineering, Università degli Studi di Palermo, Palermo, Italy

ᵇCenter for Cellular and Molecular Engineering, Department of Orthopaedic Surgery, University of Pittsburgh, Pittsburgh, PA, USA. E-mail: gottardir@chop.edu

ᶜDepartment of Bioengineering, University of Pennsylvania, Philadelphia, PA, USA

ᵈDepartment of Pulmonary and Sleep Medicine, Children's Hospital of Philadelphia, Philadelphia, PA, USA

ᵉRi.MED Foundation, Palermo, Italy

† These authors contributed equally.

‡ Present address: European Society of Clinical Microbiology and Infectious Diseases, Basel, Switzerland.

§ Present address: Institute for Tissue Engineering and Regenerative Medicine, The Chinese University of Hong Kong, Shatin, Hong Kong SAR, China.

¶ Present address: Department of Pediatrics, University of Pennsylvania and Children's Hospital of Philadelphia, Philadelphia, PA, USA.

clinic has several setbacks. Mainly, growth factors have short half-lives, diffuse rapidly from the delivery site, and are expensive.[15,16] Thus, a tissue engineering strategy to repair osteochondral defects would be more translationally feasible with less dependency on growth factors.

A translationally feasible solution to osteochondral repair must have a few key traits: promote cartilage and bone growth in the correct orientation, guide differentiation *in vivo*, be affordable and accessible, fit a short clinical timeline, and as previously mentioned, not rely on *in vivo* delivery of growth factors. The main challenge is guiding accurate spatial specification without growth factors, but current literature shows that different pore sizes can be used to guide mesenchymal stem cell differentiation.[17–21] Smaller pore sizes foster the dense cellular packing that drives chondrogenesis,[22,23] whereas inversely, larger pore sizes allow invasion of vasculature that is critical for osteogenesis.[24]

To develop a translationally feasible osteochondral repair, we used Thermally Induced Phase Separation (TIPS) to create continuous gradient porous scaffolds that range from small pore size on one end (~70 μm), to large pore sizes on the other (~200 μm). TIPS is an ideal method to create these scaffolds as the pore size and distribution can easily be changed by modulating temperature profiles and polymer concentrations,[25] as we have previously shown.[26,27] Seeded scaffolds were then placed in an established biphasic micro-physiological bioreactor system. This system allows simultaneous chondrogenic and osteogenic differentiation in the small pore side and in the large pore side, respectively, by supplying the appropriate differentiation media.[28,29] In this work, we show that TIPS can be used to create gradient porous scaffolds, and that tailored pore geometry can guide spatially relevant osteochondral differentiation of human mesenchymal stem cells (hMSCs).

Experimental

Products were purchased from Thermo Fisher Scientific (Waltham, MA) unless otherwise stated.

Scaffold design and preparation

Poly-L-Lactic Acid (PLLA) Resomer TN L 209 S (Boehringer-Ingelheim), 1,4-dioxane (Sigma-Aldrich), and distilled water were used to produce the polymeric scaffold. The ternary solution employed has a PLLA concentration of 4% wt, in 87/13% wt/wt dioxane/water (solvent/non-solvent). The system was tested to produce scaffolds *via* TIPS and the cloud point temperature for this mixture was calculated at 41 °C.[30] Different thermal histories were imposed on sample sides by an experimental apparatus made in-house using software-controlled Peltier cells.[31] After keeping the solution at 60 °C for 10 minutes (well above the cloud point), one side (Slow Cooling Side – SCS) was cooled at 1 °C min^{-1} to 30 °C and maintained for 20 minutes, whereas the other surface (Fast Cooling Side – FCS) was suddenly cooled to 30 °C and held for 50 minutes. Finally, the solution was rapidly quenched to −20 °C to freeze the obtained microstructure. To completely remove the

solvents, the polymer slabs were washed in deionized water and dried under vacuum. To further evaluate temperature variations within a sample during TIPS, the process was modelled using COMSOL multiphysics modules "heat transfer in fluids" and "phase change."

Scaffold characterization

The scaffold microstructure was observed by scanning electron microscopy (SEM) using a SEM-FEI QUANTA 200FEG. The sample cross sections were fractured in liquid nitrogen and gold sputtered for 40 s under argon. The mean pore size in each section was measured from the respective SEM image. The porosity of PLLA scaffold was evaluated *via* Boyle's pycnometer (pycnomatic ATC)[32] according to the following formula

$$\varepsilon = \frac{V_e - V_i}{V_e}$$

where ε is the porosity of the scaffold, V_e the external volume of the scaffold, and V_i the internal volume calculated by the pycnometer. Helium was adopted as a penetrating agent since its very small dimension can penetrate the smallest pores.

Micro-CT analysis (micro-CT Skyscan 1272, Bruker) was completed to acquire the 3D microarchitecture of the fabricated PLLA scaffold. Measurements were carried out at 40 kV and 250 mA, with no filter. The images were acquired with a pixel size of 6.25 μm by setting a rotation step of 0.2°. The acquired images were reconstructed with N-Recon software (version 1.6.10.2), eliminating artifacts and reducing noise in each slice. Finally, the raw image set was 3D visualized by the microCT rendering software CTVox (1.5.2 version).

Scaffold compression modulus was measured using a custom unconfined compression tester[33] with the following tests and settings: creep (time = 300 s, load limit = 2 g, ramp velocity = 10 μm s^{-1}), stress-relaxation (strain = 1%, number of ramps = 1, ramp velocity = 0.05% per s), and dynamic loading (number of cycles = 10, frequency = 0.5 Hz, amplitude = 1%). Mechanics data was analyzed using a custom MATLAB code to calculate the stress–strain curves and Young's Moduli.

Scafflod resorption and mass change was measured by first weighing the samples in their lyophilized state. Samples were then rehydrated with an ethanol gradient until 100% phosphate-buffered saline (PBS), cultured in growth media (GM) (DMEM, 10% fetal bovine serum (FBS, Invitrogen, Waltham, MA) 2% antibiotic-antimycotic (AA), 1% sodium pyruvate, 4.5 g L^{-1} D-glucose, 4 mM L-glutamine, and 25 mM HEPES) at 37 °C on a shaker at 100 rpm, and collected at D0, D2, D7, D14, and D21 post-rehydration. Collected samples were rinsed repeatedly with PBS then DI water, frozen, lyophilized, then re-weighed.

Bioreactor design and fabrication

The structures of the bioreactor were modelled using Solid-works 2014 (Dassault Systèmes, Vélizy-Villacoublay, France). All components were fabricated using a 3D Systems Viper (Rock Hill, SC) and WaterShed XC 11122 resin (DSM Somos®, Heerlen, Netherlands) as described in Nichols *et al.*[34] Accessories

include: O-Rings and tubing (McMaster-Carr, Chicago, IL), luer-locks (Cole Parmer, Vernon Hills, IL), media bags (Kiyatec, Greenville, SC), and syringes (Fisherbrand, Pittsburgh, PA).

Cell expansion

Human bone-marrow-derived mesenchymal stem cells (BM-hMSCs) were isolated from the femoral heads of patients undergoing total joint arthroplasty with IRB approval (University of Pittsburgh). This work was exempt from the requirement of informed consents as all cells were derived from surgical waste and were de-identified. All experiments were performed in accordance with federal and state regulations and guidelines. An aliquot of bone marrow was harvested, filtered through a 40 μm strainer, and the flow-through was centrifuged at 300 g for 5 min to sediment the red blood cells. The pellets were suspended using GM and plated into 150 cm^2 tissue culture flasks at a density of 10^6 cells per flask. The medium was changed every 3 to 4 days. Cells were passaged at 70–80% confluency and colony formation and trilineage mesenchymal differentiation capacity was validated before use. To obtain strong experimental evidence of the capacity of the system to promote cell differentiation, BM-hMSCs from different patients were used. Biological replicates were created by pooling BM-hMSCs at passage 3 from diverse patients: 1st Pool (1 female patient 44 years old and 2 male patients 45 and 59 years old), 2nd (1 female patient 70 years old and 2 male patients 60 and 66 years old), 3rd (1 female patient 62 years old and 2 male patients 39 and 55 years old).

Cell culture

Cylindrical scaffolds (3.5 mm diameter and 8.5 mm height) were punched out and uniformly seeded with 80 000 BM-hMSCs. Prior to seeding, the scaffolds were rehydrated and sterilized overnight in 70% ethanol then preconditioned by soaking overnight in growth medium. Constructs normalized in growth medium for 7 days prior to differentiation. Chondrogenic medium (CM: GM without FBS, +10 ng ml^{-1} TGF-β3 (PeproTech, East Windsor, NJ), 1% insulin-transferrin-selenium, 50 μM L-ascorbic acid 2-phosphate (AsA2-P), 40 μg ml^{-1} L-proline) was applied to constructs or regions undergoing chondrogenic differentiation, whereas osteogenic medium (OM: GM + 0.1 μM dexamethasone, 50 μg mL^{-1} AsA2-P, 10 mM β-glycerophosphate) was applied to constructs of regions undergoing osteogenic differentiation.

Cell proliferation assay

Cell proliferation on the PLLA gradient scaffolds was evaluated via an MTS assay (Abcam, Cambridge, England). The MTS (3-(4,5-dimethylthiazol-2-yl)-5-(3-carocymethoxyphenyl)-2-4-(sulfo-phenyl)-2H-tetrazolium) compound is reduced to a formazan product that is applied in culture medium. After incubating for 4 hours at 37 °C and 5% CO$_2$, three 100 μL samples were pipetted out from the scaffolds and absorbance was read at 490 nm. To convert the absorbance value to cell number, a preliminary calibration curve was calculated following the manufacturer's protocol.

Live/dead staining

Cell vitality of seeded scaffolds was determined after 1, 3, and 7 days. Live-dead staining was performed using Calcein-AM and ethidium homodimer-1, respectively. Seeded scaffolds were incubated in the staining solution and examined under DMi8 confocal laser scanning microscope (Leica, Wetzlar, Germany).

Gene expression

Chondral tissue from the upper part of the scaffold and osseous tissue from the lower part of the scaffold were separated. RNA was extracted using Trizol (Invitrogen, Waltham, MA) following the standard protocol after frozen hammering of the sample and purified with the RNeasy Plus mini kit (Qiagen, Hilden, Germany). SuperScript III kit (Invitrogen, Waltham, MA) was utilized with random hexamer primers to complete the reverse transcription. Real-time RT-qPCR was performed using the StepOnePlus thermocycler (Applied Biosystems, Foster City, CA) and SYBR Green Reaction Mix (Applied Biosystems, Foster City, CA). 18S was used as the housekeeping gene and the various gene expression levels were calculated using the comparative Ct method. SRY-box transcription factor (SOX9), aggrecan (ACAN), and collagen type 2 (COL2A1) were used as indicative genes for cartilage. Runt-related transcription factor 2 (RUNX2), bone sialoprotein 2 (BSP2), and osteopontin (OPN) were used as indicative genes for bone. The gene sequences are depicted in Table 1.

Histology

Scaffolds were fixed in 10% paraformaldehyde overnight, dehydrated, and embedded in paraffin. The embedded samples were sectioned at 10 μm, mounted on slides and subsequently processed and stained. Alcian blue and Alizarin red staining were used to detect the glycosaminoglycan (GAG) production by chondrocytes and calcium deposition by osteoblasts, respectively.

Table 1 Primers for RT-qPCR

| Gene	Forward (5′–3′)	Reverse (5′–3′)
18S	GTAACCCGTTGAACCCCATT	CCATCCAATCGGTAGTAGCG
SOX9	CTGAGCAGCGACGTCATCTC	GTTGGGCGGCAGGTACTG
ACAN	GCTACACTGGCGAGCACTGTAACAT	GCGCCAGTTCTCAAATTGCATGGG
COL2A1	GGATGGCTGCACGAAACATACCGG	GGATGGCTGCACGAAACATACCGG
RUNX2	CAACCACAGAACCACAAGTGCG	TGTTTGATGCCATAGTCCCTCC
BSP2	CGAATACACGGGCGTCAATG	GTAGCTGTACTCATCTTCATAGGC
OPN	TCACCAGTCTGATGAGTCTCACCATTC	TAGCATCAGGGTACTGGATGTCAGGT
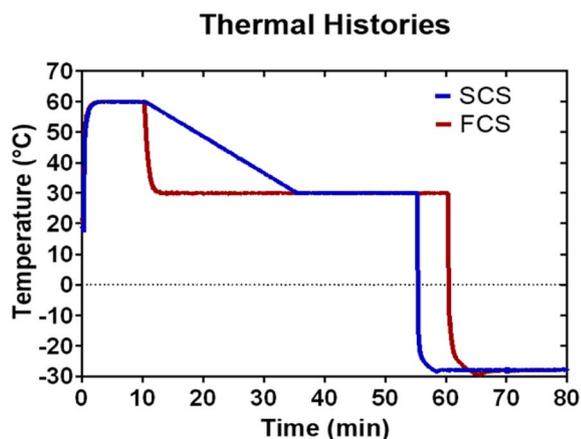
Fig. 1 Thermal histories of the Slow Cooling Side (SCS) and Fast Cooling Side (FCS) used to create the gradient porous PLLA scaffold.

Statistical analysis

All graph results expressed as mean ± standard deviation. Individual points are representative of different donor pools. Graphs were created and data was analyzed using GraphPad Prism 10. Mechanics data in Fig. 3 and cell viability data for Fig. 4 were analyzed using a one-way ANOVA. PCR data for Fig. 6 was analyzed by a 2way ANOVA test with matched values, mixed-effects model, and Fisher's LSD test for multiple comparisons.

PCR data for Fig. 7 was analyzed using a paired Wilcoxon Test. Scaffold resorption data in SI, Fig. S1 was analysed using one-way ANOVA at day 7, and one sample T-tests at each time point compared to dry scaffolds. Statistical significance is determined at $p < 0.05$ (*), $p < 0.01$(**), $p < 0.001$(***), $p < 0.0001$(****).

Results

Development of a continuous gradient porous scaffold for osteochondral repair

Scaffold design and preparation. PLLA scaffolds were formed by TIPS with the thermal histories depicted in Fig. 1. COMSOL modelling of the scaffold was used to analyze heat transfer during the TIPS process and guide the parameters needed to achieve different pore sizes at each end of the scaffold. The three-dimensional system was considered with a one-dimensional change, given the symmetry of the geometry (a rectangular prism with 1 cm width, 3 cm depth, and 3.5 cm height, which matches the dimension used during TIPS). The thermal history was applied to the 3 cm by 3.5 cm side, and the other sides were simulated as external natural convection. The outside fluid was 20 °C air, and the simulation fluid was 87%/13% wt/wt dioxane/water. Two thermal histories were reported to represent the system behaviour. The first thermal history is a step input from 60 °C to 35 °C to simulate the internal temperature profiles inside the fluid region. The second one is
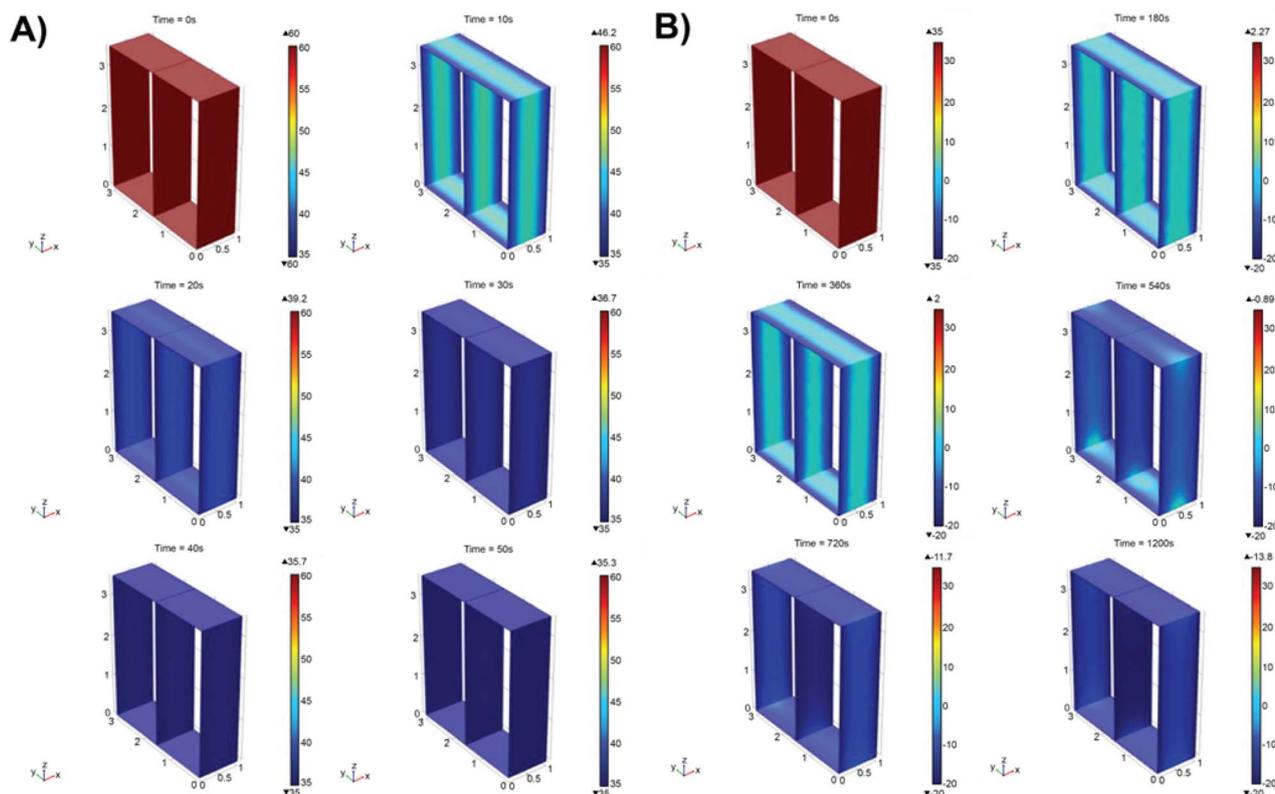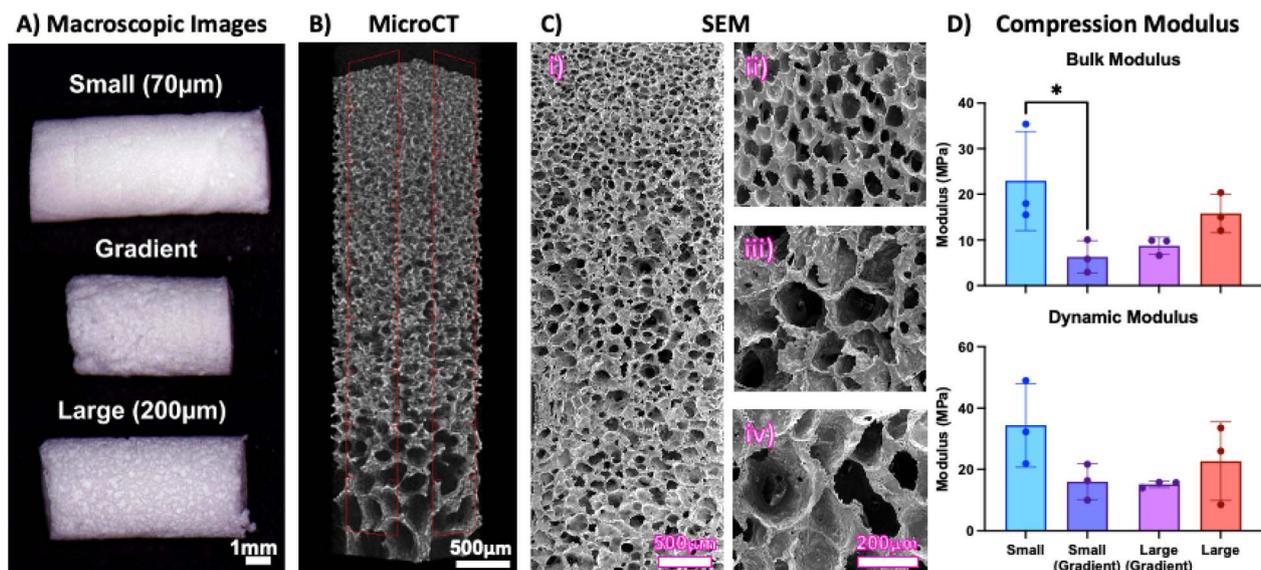

Fig. 2 COMSOL modelling analysing heat transfer throughout the scaffold at (A) above freezing and (B) during a phase change and subsequent freezing.

Fig. 3 Scaffold characterization: (A) macroscopic image of the different porous scaffolds. (B) MicroCT reconstruction showing pore network of the gradient scaffold. (C) SEM micrograph showing (i) pore sizes along the length of the scaffold and magnified images of (ii) small pores ~70 μm, (iii) middle pores ~150 μm, and (iv) large pores ~200 μm. (D) Compressive modulus of the small pore scaffolds, large pore scaffold, and the small and large pore regions of the continuous gradient scaffold.

a step input from 35 °C to −20 °C, to show the temperature profiles when a phase change occurs. In both cases, temperature profiles on the external surface and in a "virtual" surface at the center of the samples were reported.

Fig. 2A shows that at $t = 10$ s, the temperature spans from 35 °C on one side of the slab to 46.2 °C at the center. It is possible to see that almost 500 μm of the slab is above 40 °C. At $t = 20$ s, the entire system is under 40 °C. The entire process can be considered concluded by $t = 30$ s.

The phenomenon is completely different when a phase change occurs (Fig. 2B). More time is required for the system to reach the desired temperature. At $t = 180$ s, the 3 cm by 3.5 cm edges reach the set point quickly, while the freezing process occurs at the rest the system. By $t = 720$ s, the system is fully frozen and steady state is reached by $t = 1200$ s.

Scaffold characterization. Fig. 3A shows macroscopic images of the small, large, and gradient pore scaffold. MicroCT reconstruction (Fig. 2B) shows the pore network, highlighting that it is highly porous and interconnected. Fig. 3C shows the SEM micrograph of the PLLA scaffold. The compressive moduli of the scaffolds show that for both bulk and dynamic, the single pore-size scaffolds are stiffer, with the small pores being the stiffest. Importantly, all moduli are in the MPa range, which is stronger than other scaffold formulations and closer to the *in vivo* range.[35] Scaffold resorption (SI, Fig. S1) was negligible compared to salt deposition and protein adsorption in the given time scale.

The fast-cooling side (FCS) had an average pore diameter of 200 μm, and the slow-cooling side (SCS) had an average pore diameter of 70 μm. Previous studies about TIPS have highlighted that, when a nucleation-and-growth mechanism occurs,
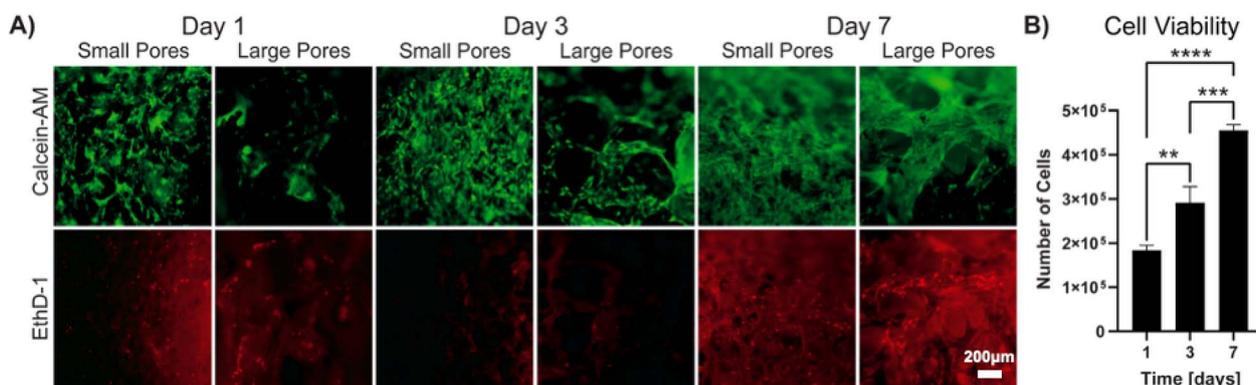
Fig. 4 Gradient porous scaffold is non-cytotoxic and allows cell growth: (A) Calcein AM and ethidium homodimer-1 staining of the scaffold over 7 days to show live and dead cells. (B) MTS assay showed significant proliferation of cells on the scaffold over 7 days.
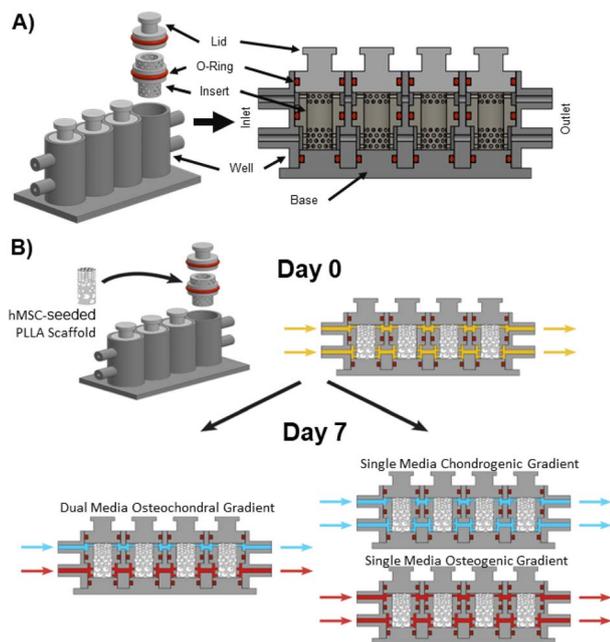
Fig. 5 Schematic showing (A) bioreactor components and structure and (B) experimental set up.

the pore dimension is primarily dictated by the thermal history.[36] Thus, by varying the residence time in the metastable region, it was possible to control the pore dimension. The FCS spent more time in the metastable region than the SCS, so it was expected that the pore dimensions in the FCS are larger than the SCS. This allowed for a gradual change of pore dimension along the sample thickness. The porosity, evaluated *via* gas pycnometer, was $93 \pm 0.5\%$ in the whole scaffold.

Cell viability. Live-dead staining of the BM-hMSCs in the PLLA scaffold at days 1, 3, and 7 are shown in Fig. 4A. An MTS assay was used to calculate cell numbers in the scaffold (Fig. 4B). A cell seeding efficiency of $22.8\% \pm 1.3\%$ is reported, and the cell counts more than double after 7 days, showing that the scaffold supports cell proliferation and there is no PLLA cytotoxicity.

Continuous gradient porous scaffold support osteochondral differentiation

Bioreactor and experimental layout. This bioreactor has been developed to replicate *in vitro* the physiological conditions of osteochondral tissue. A main problem with the reproduction of the osteochondral unit is the difficulty to supply distinct differentiation media to the same complex. The divergent environments in which cartilage and bone develop are a particularly troubling hurdle to overcome. Features such as growth factors and supplements, oxygen, pH, and mechanical stimulation are known to be important to histogenesis and tissue-specific formation for bone and cartilage. The bioreactor was designed to allow delivery of specific signalling cues to each side of a construct. As illustrated in Fig. 5A, the bioreactor is composed of four cells. Each cell contains a perforated removable insert, where the scaffold is placed. A detachable base under the wall facilitates the removal of the insert. A silicone O-ring around the insert divides the cell into two chambers and provides a leak-proof seal. Two channels, under and above the insert O-ring, allow the provision of specific media. The channels are connected to syringes in a syringe pump and collection bags: the former to supply the media, the latter to collect the spent media.
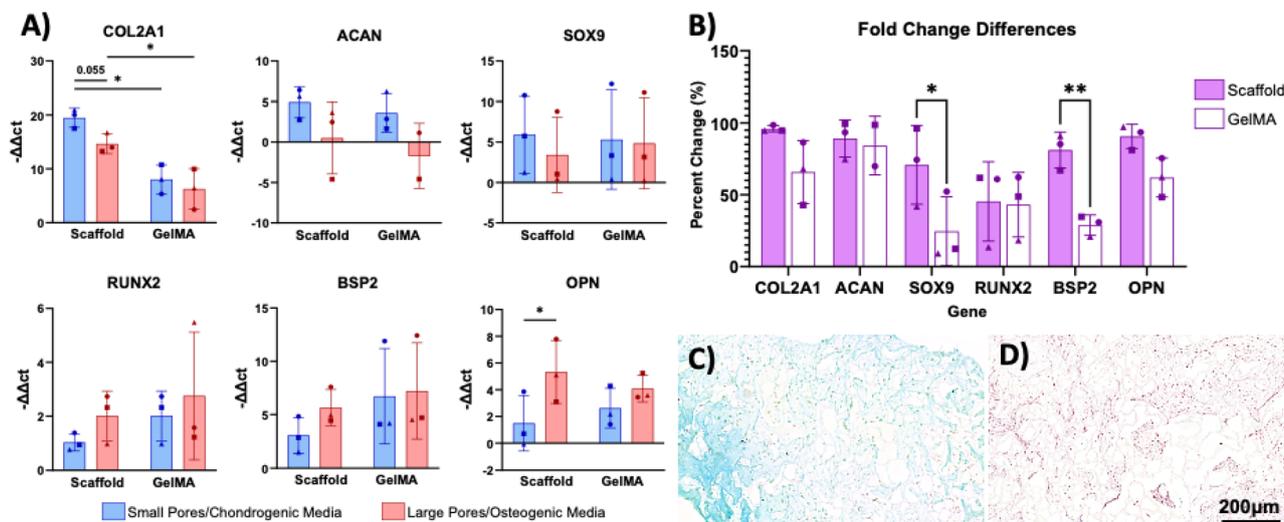

Fig. 6 Gradient porous PLLA scaffold cultured biphasically in the bioreactor generates an osteochondral construct: (A) RT-qPCR data showing expression of chondrogenic and osteogenic genes in the scaffold and GelMA control in the small pore/chondrogenic side *versus* the large pore/osteogenic side. (B) Percent of the change between the small pore/chondrogenic side *versus* the large pore/osteogenic side normalized to the larger value. (C) Alcian blue staining of the small pore/chondrogenic side (scale = 200 μm). (D) Alizarin red staining of the large pore/osteogenic side (scale = 200 μm).

Gradient PLLA scaffolds were seeded with cells, placed into the bioreactor with the small pore side upward, and perfused with growth medium (GM) for 7 days. On day 7, the medium for dual media osteochondral gradient experiments (Fig. 5B) was switched to chondrogenic medium (CM) in the upper chamber and osteogenic medium (OM) in the lower chamber. Simultaneous osteochondral biphasic differentiation of the gradient scaffold was performed to validate the ability to generate an osteochondral construct representative of native biology. The gradient scaffolds were also cultured with single media conditions to tease out the effect of the pore sizes on differentiation under the same conditions. Following the same timeline, the medium for single medium chondrogenic gradient experiments and single medium osteogenic gradient experiments was switched to CM and OM respectively. The constructs were differentiated for 3 weeks. All media was perfused at a rate of 80 µL h^{-1}. After the experiment, the scaffolds were pushed out of the insert using a simple 3D printed plunger tool and processed for gene expression analysis or histochemical evaluation.

Dual media osteochondral gradient PCR and histology. The scaffolds were cut in two parts, corresponding to chondral (small pore, CM) and osseus (large pore, OM) region and each part was analyzed *via* RT-qPCR. The values are reported as fold changes from day 0 and 18S are compared to methacrylated gelatin (GelMA, non-porous control) scaffolds that underwent the same experimental conditions (Fig. 6A). In the chondrogenic region, the data showed upregulation of chondrogenic genes *COL2* in the scaffold group *versus* the GelMA group. Conversely, in the osteogenic region, the data showed significant upregulation of osteogenic gene *OPN* in the scaffold group *versus* the GelMA group. Additionally, there was significantly greater *COL2* expression in the scaffold *versus* the GelMA control. Percent change of gene expression fold change (FC) (Fig. 6B) between the chondral region and the osseus region of each construct for chondrogenic genes was calculated as:

$$\%\text{Change} = \frac{|\text{FC (chondral)} - \text{FC (osseus)}|}{\text{FC(chondral)}} \times 100\%$$

For osteogenic genes, the regions in the equation were switched. For all genes, the scaffold groups showed a greater percent change between the chondral and osseus region than the GelMA groups, significantly so for *SOX9* and *BSP2*, strongly suggesting that the varying pore sizes provide differentiation cues beyond those afforded by the differentiation media. Although the statistical significance in the reported data is limited, given the relatively small donor sample size and the well-known variability of human donors, we found the observable trend indicative of the changes induced by the scaffold pore sizes.

Fig. 6C shows Alcian blue staining for GAGs of the chondral region of the PLLA scaffold, and Fig. 6D shows Alizarin red staining for calcium of the osseus region of the PLLA scaffold.
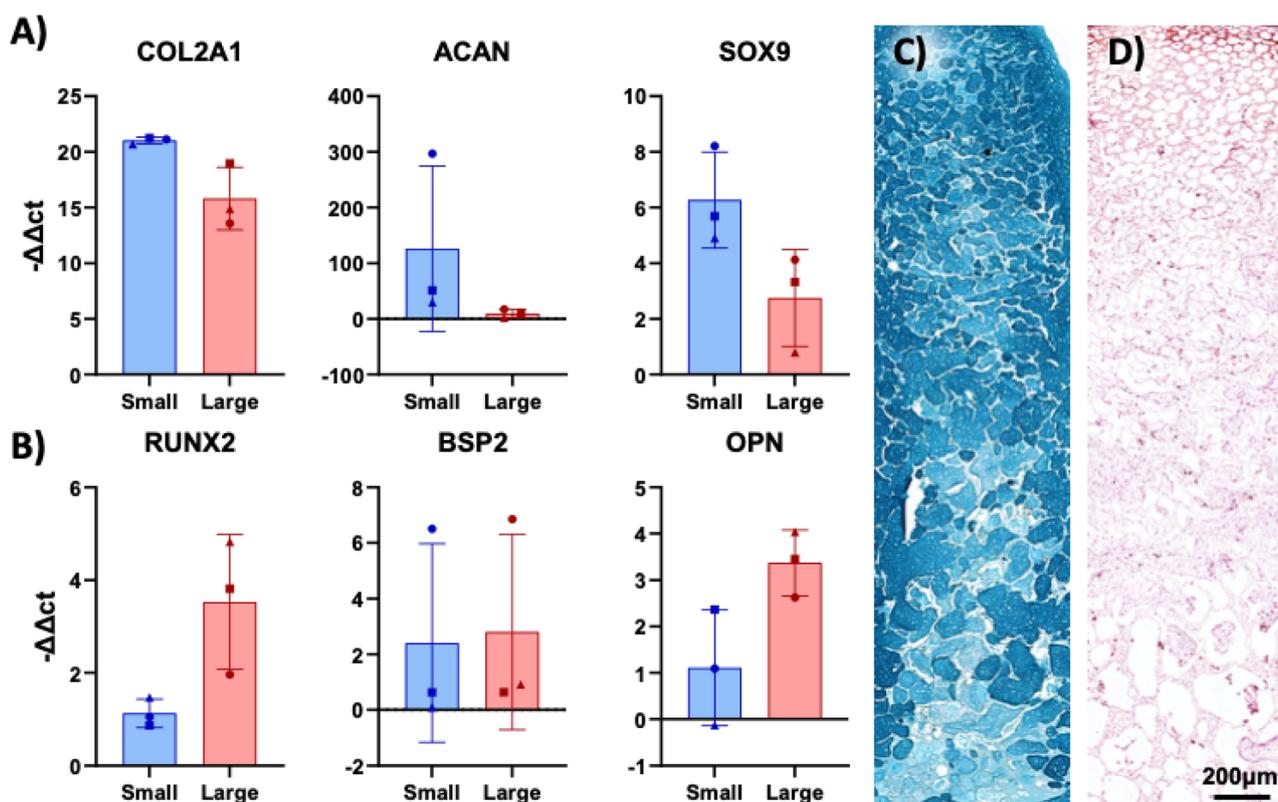

Fig. 7 Pore sizes drive local differentiation even in identical media conditions: (A) RT-qPCR data showing expression of chondrogenic genes in the small pore *versus* the large pore region under chondrogenic conditions. (B) RT-qPCR data showing expression of osteogenic genes in the small pore *versus* the large pore region under osteogenic conditions. (C) Alcian blue staining of gradient scaffold under chondrogenic conditions (scale = 200 µm). (D) Alizarin red staining of the gradient scaffold under osteogenic conditions (scale = 200 µm).

Strong presence of GAGs and calcium indicated that differentiation is supported in the respective regions of the PLLA scaffold.

Single medium chondrogenic/osteogenic gradient PCR and histology. Single medium experiments, in which both sides of the gradient scaffold were exposed to the same medium, were carried out to discover how pore sizes affect the differentiation profile. Adopting the same protocol of previous test, the scaffold was cut in two parts, the small pore region and the large pore region. For scaffolds treated with CM, the small pore side showed upregulation of chondrogenic genes (Fig. 7A), and the inverse is true for the scaffolds treated with OM (Fig. 7B). Alcian blue staining of the scaffold treated with CM showed higher GAG presence in the small pore side (Fig. 7C), and Alizarin red staining of the scaffold treated with OM showed higher calcium deposition in the large pore size (Fig. 7D). In conclusion, small pores helped drive chondrogenic differentiation and resist calcification, leading to a robust cartilage phenotype at the chondral side of the osteochondral construct. This trend may be due to increased contact between cells in the small pores. The larger pores required more cells to fill the entire free space than the smaller pores.[37,38] Filling the pores can increase the cell–cell interactions and simulate high density, providing a good three-dimensional microenvironment to promote chondrogenic differentiation and cartilage tissue formation.[39]

Discussion

The objective of this study was to develop a scaffold for osteochondral defect repair that can drive local cell fate through surface topography. An ideal scaffold could be implanted *in vivo* and intrinsically drive tissue specific repair. This can be difficult to achieve in the osteochondral junction, as there are different tissue types throughout the tissue. Thus, we proposed a gradient porous scaffold to promote stem cell differentiation through pore geometry, so that it is less dependent on external factors such as growth factors, which are translationally challenging.[14–16]

We first developed and characterized the PLLA scaffold, showing that we can use TIPS to control the range of pore sizes from about 70 μm to about 200 μm. We chose to use PLLA as our polymer, since PLLA is biodegradable, has lower cytotoxicity than other synthetic polymers,[40] and – when synthesized with low polydispersity – allows for tight control of nucleation using the previously described TIPS method. PLLA is both biodegradable, meaning that the polymer structure breaks down, and bioabsorbable, meaning that the body can excrete the broken down components.[41] PLLA can take almost 2 year to completely degrade,[41,42] leaving ample time for tissue regeneration to replace the scaffold and fill the defect. Critically, while PLLA can cause a minor foreign body response as do most biomaterials,[43] *in vitro* and *in vivo* experiments have shown minimal long-term inflammatory responses to PLLA-based biomaterials.[44] *In vitro* and *in vivo* assays show that PLLA-based biomaterials do not cause hemolysis.[41,42] These qualities of PLLA justify why it has been successfully used as a biomaterial in both cartilage and bone tissue engineering.[45–48] Ma *et al.* seeded chondrocytes on a PLLA and collagen scaffold and showed high cell proliferation

and spreading.[49] Liu *et al.* used PLLA nanofiber scaffolds as a base with piezoelectric charge and mechanical activation to repair hyaline cartilage in a rabbit model.[50] Similarly, Polak *et al.* used piezoelectric, electrospun PLLA fibrous scaffolds to increase adhesion of osteoblasts.[51] Ciapetti *et al.* mixed PLLA with various biomimetic cues to increase osteoconduction of MSCs,[52] and Meng *et al.* mixed PLLA with PCL to generate membranes that promote adhesion and proliferation of osteoblasts.[53] Previous work from our group showed that PLLA mixed with hydroxyapatite to promote bone differentiation can still undergo TIPS.[48] Thus, PLLA is an ideal polymer for our system and has been previously shown to be successful in osteochondral tissue engineering.

For this study, focused on the role of pore size in supporting stem cell differentiation, we choose to use only PLLA in our scaffold, with pore sizes ranging from ∼70 μm to ∼200 μm to drive differentiation of MSCs into cartilage and bone, respectively. We chose to direct pore size to this specific diameter based on previous literature. In fact, geometry has been shown to direct stem cell fate and differentiation.[26,54–56] Kilian *et al.* seeded stem cells on patterned adhesive islands of different shapes, showing that higher aspect ratio shapes promoted greater contractility and in turn, greater osteogenesis over adipogenesis.[57] Specifically, it has been shown that smaller pores, can drive chondrogenic differentiation and matrix deposition. Our previous work using similar methods shows that PLLA scaffolds with 100 μm pores drives more chondrogenesis than 200 μm pores.[26] Additionally, Zeng *et al.* used alginate hydrogels with microcavities to show that their smallest pore size promoted both cell proliferation and chondrogenic extracellular matrix synthesis.[58] Duan *et al.* determined that pore sizes of 100–200 μm were optimal for cartilage growth, and sizes of 300–450 μm were optimal for bone growth.[59] Similarly, Di Luca *et al.* showed that decreasing pore sizes drive chondrogenesis[60] and that increasing pore sizes drive osteogenesis.[61] We used this preexisting information and our preliminary experiments to determine the range of pores in our monolithic PLLA scaffold.

To achieve fine control of the pores in our scaffold, along with a continuous gradient, we determined that TIPS was the best method to generate our scaffold. TIPS can generate scaffolds that are highly porous and have an interconnected network of pores, ideal for recellularization. Our previous work has shown the capabilities of tuning pore size and structure of polymers using TIPS.[27] Another benefit of TIPS is its clinical translatability, as it is highly scalable and an inexpensive production process.[25] However, we wanted our scaffold to have a continuous gradient of pore sizes, instead of two distinct regions, to avoid the risk of delamination[62–64] and more accurately represent the multilayer organization of the osteochondral junction.[45] Specifically, we aimed to perform TIPS simultaneously with two different cooling profiles at either end of the PLLA slab. We used a previously described custom apparatus made in-house using two Peltier cells with heat sinks.[48] The fast-cooling side created large pores, the slow-cooling side created small pores, and the pore size smoothly transitioned in between. Thus, we have a translatable procedure

to create continuous porous gradient scaffolds in principle capable of enhancing stem cell differentiation.

To validate our scaffold *in vitro*, we used our established biphasic bioreactor to simultaneously differentiate the small-pore side chondrogenically, and the large-pore side osteogenically.[65] The bioreactor allows perfusion of two different media streams with no mixing except through diffusion within the construct.[29] This way, we can create *in vitro* two separate microenvironments representative of the native osteochondral junction.

We first considered cell adhesion, viability, and proliferation on the PLLA scaffold. PLLA is considered hydrophobic, which can warrant concerns about cell attachment.[40,66] To overcome this, we preconditioned the scaffold by soaking it overnight in growth medium containing 10% FBS. The adsorbed protein and nutrients help drive cell infiltration and adhesion. While an FBS soak is not clinically translatable, we have also confirmed cell attachment and growth after preconditioning the scaffold in gelatin, collagen, or fibronectin (data not shown). These matrix proteins are well studied and already approved for clinic use in other application.[67–70] We visualized the efficacy of the preconditioning using live-dead staining with Calcein-AM and ethidium homodimer 1, and MTS assay, seeing steady growth of cells on both pore sizes of the scaffold over 7 days, confirming cellularization, compatibility, and non-toxicity. We then placed the seeded PLLA scaffold into the bioreactor and perfused the small pore side with chondrogenic media and the large pore side with osteogenic media. We differentiated the scaffold for 3 weeks to validate our ability to generate an osteochondral construct. RT-qPCR for chondrogenic genes *COL2*, *ACAN*, and *SOX9*, and osteogenic genes *RUNX2*, *BSP2*, and *OPN*, showed upregulation of chondrogenic gene *COL2* in the scaffold in the small pore region *versus* the large pore region and significant upregulation of *OPN* in the large pore region *versus* the small pore region, indicating a differential cellular specification. We also seeded cells in a GelMA scaffold, cultured in the same way, to act as a control with uniform topography and no pores. Notably, we did not see significant upregulation of *COL2* in the upper chamber *versus* the lower chamber of the GelMA control, hinting that the PLLA scaffold positively affects differentiation. We also saw significantly greater *COL2* expression in the scaffold *versus* the GelMA control, suggesting the PLLA porous scaffolds can promote chondrogenesis greater than the hydrogel. We then stained for glycosaminoglycans, abundant in cartilage, with Alcian blue, and for calcium deposition, indicative of bone calcification, with Alizarin red. As expected, we saw more robust Alcian blue signal in the small pore region, and more abundant Alizarin red signal in the large pore region, with both stains stronger in the PLLA scaffold *versus* the corresponding GelMA control (SI, Fig. S2). To summarize these results, we compared the percent change of the PCR fold change results to show that there is greater difference in differentiation between the small pore/chondrogenic region and the large pore/osteogenic region in the PLLA scaffold *versus* the GelMA control. The difference of *SOX9* expression and *BSP2* expression is significantly greater in the PLLA scaffold than the GelMA

control. This data implies that pores may play a critical role in driving differentiation.

To further determine the capabilities of pore size to drive differentiation, we then perfused a gradient scaffold with only CM or only OM and performed the same assays to look for difference due solely to pore size. We saw significant upregulation of *COL2* in the small pore region *versus* the large pore region, indicating that the small pores enhance chondrogenic differentiation. We also saw a higher fold change of *RUNX2* and *OPN*, albeit with high variability, suggesting that the small pores are not conductive to ossification even when exposed to osteogenic conditions. Histologically, we saw Alcian blue signal throughout the scaffold, with greater signal in the small pore region. Inversely, we saw Alizarin red signal primarily in the large pore region. The absence of calcium deposition in the small pore region w promising, as a great shortcoming of tissue engineered cartilage is its tendency to calcify.[6,8]

We have shown that our gradient porous scaffold can support local differentiation of stem cells into chondrogenic and osteogenic phenotypes, with the end goal of clinically translational osteochondral defect repair. Multi-tissue repair is a common concern, as few tissues operate in isolation *in vivo*. To work towards a solution, many researchers have proposed gradient scaffolds of their own. These gradients can be discrete or continuous, and can be a change in mechanical properties, biochemical components, or porosity, and can be achieved in many ways. Zhu *et al.* created a gradient scaffold for tendon repair by modulating crystallinity and microstructure of poly-vinyl alcohol (PVA) along the length of the hydrogel.[71] Du *et al.* used laser sintering to create a continuous cartilage-bone scaffold with poly(ε-caprolactone) (PCL) microspheres and PCL/hydroxyapatite microspheres, respectively.[72] Wei *et al.* used multiple techniques to develop a successful layered hydrogel scaffold for osteochondral defect repair.[73,74] A sodium alginate/gelatin hydrogel layered on a sodium alginate/gelatin and β-tricalcium phosphate hydrogel created different matrices for cartilage and bone growth respectively. There was also a gradient of kartogenin and pore sizes to further drive tissue specific differentiation. Evidently, there are many creative ways to develop gradient scaffolds for multiple tissue repair, and many researchers have had success. The benefit of our approach is that it is clinically translatable; it is affordable, easy to fabricate, and has potential for off-the-shelf applications. Additionally, the continuous nature of the gradient adds mechanical stability, as delamination is less likely to occur.[75]

A limitation of the study was the lack of significant changes in the osteogenic region of the scaffold. During osteogenesis, the OM only contained β-glycerophosphate as a morphogen that drives osteogenesis.[76–78] While this is effective in 2D osteogenic assays, it is a weak morphogen in 3D differentiation. This is acceptable in our *in vitro* study aimed at exploring the role of pore size, however it would not be ideal for differentiation prior to *in vivo* deployment. The addition of Vitamin D3 [79–81] or BMPs[82] could help drive further osteogenesis during differentiation prior to *in vivo* implantation. Another question to consider is whether the PLLA scaffold can initiate differentiation with no chondro- or osteoinductive factors present. We

expect that some initial morphogenic trigger might be necessary, in much the same way as TGF-β is necessary for cartilage formation during mesenchymal condensation in development.[47] While beyond the scope of this study, we plan to test these conditions in preparation for our future *in vivo* studies.

While we have shown that small pores specifically contribute to chondrogenesis, an open question remains on the specific mechanism at play. We hypothesize that the small pores aid in chondrogenesis due to either hypoxia or by mimicking mesenchymal condensation. Small pores and tightly packed cells may limit the diffusion of gases and nutrient,[22] including oxygen, and hypoxic conditions are known to enhance chondrogenesis.[83] We hypothesize that at the same time, the small pores may effectively drive chondrogenesis by packing the cells together and creating a mesenchymal condensation-state. This process would be particularly interesting as the mechanisms of mesenchymal condensation are an active area of study[84,85] as well as their application for chondrogenesis.[86–88] In future studies, we plan to specifically dissect the contribution of hypoxia *versus* a condensation-like state to chondrogenesis in the small pore scaffolds.

Conclusions

We observed a spatially defined, biphasic differentiation of hMSCs within the engineered PLLA scaffold for osteochondral constructs. The pore gradient scaffold is obtained in a single fabrication step, using a single material, by thermally induced phase separation. This technique allowed for the fabrication of a gradient scaffold with a pore dimension appropriate to replicate the osteochondral junction from cartilage (70 micron) to bone (200 micron). Furthermore, the different cell types (chondrocytes and osteoblasts) are obtained from bone marrow derived hMSCs that are commonly used in cartilage and bone engineering and are the resident progenitor cells in osteochondral defect repair. A single unit biodegradable scaffold produced with local gradient pore structure may then be tailored for chondro- and osteoinduction and applied to improve osteochondral tissue repair, providing mechanical stability and local cues for cell differentiation.

Author contributions

GC: conceptualization, data curation, formal analysis, investigation, methodology, project administration, software, validation, visualization, writing – original draft. KWYS: data curation, formal analysis, investigation, project administration, validation, writing – original draft, writing – review & editing. AP: conceptualization, investigation, validation, methodology. FCP: conceptualization, investigation. EYZ: investigation, validation. VLC: conceptualization, funding acquisition, supervision. VB: conceptualization, funding acquisition, supervision. RST: conceptualization, funding acquisition, resources, supervision. RG: conceptualization, data curation, funding acquisition, project administration, resources, writing – review & editing.

Conflicts of interest

RST and RG are co-inventor of an issued patent for the biphasic bioreactor technology.

Data availability

The data supporting this article have been included as part of the SI.

The supplementary information includes SI data for scaffold adsorption/resorption, histology of GelMA controls, COMSOL analysis files, mechanics raw data and analysis code, RT-qPCR raw data, MTS raw data, thermal history raw data, thermal history analysis code. See DOI: https://doi.org/10.1039/d5ra00540j.

Acknowledgements

Notes and references

1 D. C. Flanigan, J. D. Harris, T. Q. Trinh, R. A. Siston and R. H. Brophy, *Med. Sci. Sports Exercise*, 2010, **42**(10), 1795–1801.

2 P. Graham, *Orthop. Nurs.*, 2017, **36**, 237–239.

3 N. Bhardwaj, D. Devi and B. B. Mandal, *Macromol. Biosci.*, 2015, **15**, 153–182.

4 M. Howell, Q. Liao and C. W. Gee, *Curr. Rev. Musculoskelet Med.*, 2021, **14**, 60–66.

5 I. Martin, D. Schaefer and B. Dozin, in *Madame Curie Bioscience Database [Internet]*, Landes Bioscience, 2013.

6 A. R. Armiento, M. Alini and M. J. Stoddart, *Adv. Drug Deliv. Rev.*, 2019, **146**, 289–305.

7 B. F. Mandell, *Synovial Fluid Analysis and The Evaluation of Patients With Arthritis*, 2022.

8 S. Muthu, J. V. Korpershoek, E. J. Novais, G. F. Tawy, A. P. Hollander and I. Martin, *Nat. Rev. Rheumatol.*, 2023, **19**, 403–416.

9 M. Sarsenova, Y. Raimagambetov, A. Issabekova, M. Karzhauov, G. Kudaibergen, Z. Akhmetkarimova, A. Batpen, Y. Ramankulov and V. Ogay, *Polymers*, 2022, **14**, 5343.

10 L. S. Lohmander, S. Hellot, D. Dreher, E. F. W. Krantz, D. S. Kruger, A. Guermazi and F. Eckstein, *Arthritis Rheumatol.*, 2014, **66**, 1820–1831.

11 S. S. Shah and K. Mithoefer, *Curr. Rev. Musculoskelet. Med.*, 2020, **13**, 641–650.

12 X. Ren, M. Zhao, B. Lash, M. M. Martino and Z. Julier, *Front. Bioeng. Biotechnol.*, 2020, **7**, 1–9.

13 N. A. Householder, A. Raghuram, K. Agyare, S. Thipaphay and M. Zumwalt, *Orthop. J. Sports Med.*, 2023, **11**, 23259671231155950.

14 K. B. McGowan and G. Stiegman, *Cartilage*, 2013, **4**, 4–11.

15 H. Huang, Z. Lou, S. Zheng, J. Wu, Q. Yao, R. Chen, L. Kou and D. Chen, *Drug Deliv.*, 2022, **29**, 767–791.

16 B. Sridharan, B. Sharma and M. S. Detamore, *Tissue Eng., Part B*, 2016, **22**, 15–33.

17 M. J. Gupte, W. B. Swanson, J. Hu, X. Jin, H. Ma, Z. Zhang, Z. Liu, K. Feng, G. Feng, G. Xiao, N. Hatch, Y. Mishina and P. X. Ma, *Acta Biomater.*, 2018, **82**, 1–11.

18 C. M. Murphy, G. P. Duffy, A. Schindeler and F. J. O'Brien, *J. Biomed. Mater. Res., Part A*, 2016, **104**, 291–304.

19 P.-Y. Wang, L. R. Clements, H. Thissen, W.-B. Tsai and N. H. Voelcker, *Biomater. Sci.*, 2013, **1**, 924.

20 P. Y. Wang, H. Thissen and P. Kingshott, *Acta Biomater.*, 2016, **45**, 31–59.

21 C. Bettinger, R. Langer and J. Borenstein, *Angew. Chem., Int. Ed.*, 2009, **48**, 5406–5415.

22 M. M. Nava, L. Draghi, C. Giordano and R. Pietrabissa, *J. Appl. Biomater. Funct. Mater.*, 2016, **14**, e223–e229.

23 T. H. Lin, H. C. Wang, W. H. Cheng, H. C. Hsu and M. L. Yeh, *Int. J. Mol. Sci.*, 2019, **20**(2).

24 S. Nadine, I. J. Fernandes, C. R. Correia and J. F. Mano, *iScience*, 2022, **25**, 105370.

25 R. Zeinali, L. J. Del Valle, J. Torras and J. Puiggalí, *Int. J. Mol. Sci.*, 2021, **22**(7).

26 G. Conoscenti, T. Schneider, K. Stoelzel, F. Carfì Pavia, V. Brucato, C. Goegele, V. La Carrubba and G. Schulze-Tanzil, *Mater. Sci. Eng., C*, 2017, **80**, 449–459.

27 F. Carfì Pavia, V. La Carrubba, S. Piccarolo and V. Brucato, *J. Biomed. Mater. Res., Part A*, 2008, **86**, 459–466.

28 A. Pirosa, R. Gottardi, P. G. Alexander, D. Puppi, F. Chiellini and R. S. Tuan, *Biomaterials*, 2021, **272**.

29 L. Iannetti, G. D'Urso, G. Conoscenti, E. Cutrì, R. S. Tuan, M. T. Raimondi, R. Gottardi and P. Zunino, *PLoS ONE*, 2016, **11**(9).

30 G. A. Mannella, F. Carfì Pavia, G. Conoscenti, V. La Carrubba and V. Brucato, *J. Polym. Sci., Part B: Polym. Phys.*, 2014, **52**, 979–983.

31 G. A. Mannella, G. Conoscenti, F. Carfì Pavia, V. La Carrubba and V. Brucato, *Mater. Lett.*, 2015, **160**, 1–4.

32 I. Zein, D. W. Hutmacher, K. C. Tan and S. H. Teoh, *Biomaterials*, 2002, **23**, 1169–1185.

33 R. L. Mauck, M. A. Soltz, C. C. B. Wang, D. D. Wong, P.-H. G. Chao, W. B. Valhmu, C. T. Hung and G. A. Ateshian, *J. Biomech. Eng.*, 2000, **122**, 252–260.

34 D. A. Nichols, I. S. Sondh, S. R. Litte, P. Zunino and R. Gottardi, *Biomed. Microdevices*, 2018, **20**, 4–11.

35 Y. J. Hu, Y. E. Yu, H. J. Cooper, R. P. Shah, J. A. Geller, X. L. Lu, E. Shane, J. Bathon, N. E. Lane and X. E. Guo, *J. Bone Miner. Res.*, 2024, **39**, 1120–1131.

36 L. He, Y. Zhang, X. Zeng, D. Quan, S. Liao, Y. Zeng, J. Lu and S. Ramakrishna, *Polymer*, 2009, **50**, 4128–4138.

37 M. Hirao, N. Tamai, N. Tsumaki, H. Yoshikawa and A. Myoui, *J. Biol. Chem.*, 2006, **281**, 31079–31092.

38 T. D. Bornes, N. M. Jomha, A. Mulet-sierra and A. B. Adesida, *Stem Cell Res. Ther.*, 2015, **6**(84).

39 M. Zhu, Q. Feng and L. Bian, *Acta Biomater.*, 2014, **10**, 1333–1340.

40 E. Capuana, F. Lopresti, M. Ceraulo and V. La Carrubba, *Polymers*, 2022, **14**, 1153.

41 M. Xavier, N. Farez, P. L. Salvatierra, A. L. Jardini, P. Kharmandayan and S. Feldman, *F1000Research*, 2021, **10**, 1275.

42 P. Wang, M. Wang, X. Wei, L. Xie, L. Tian, Z. Yang, Z. Zhou and H. Chen, *Int. J. Biol. Macromol.*, 2024, **272**, 132876.

43 M. Nonhoff, J. Puetzler, J. Hasselmann, M. Fobker, G. Gosheger and M. Schulze, *Polymers*, 2024, **16**, 817.

44 D. L. Biggs, C. S. Lengsfeld, B. M. Hybertson, K. Ng, M. C. Manning and T. W. Randolph, *J. Controlled Release*, 2003, **92**, 147–161.

45 P. Nooeaid, V. Salih, J. P. Beier and A. R. Boccaccini, *J. Cell. Mol. Med.*, 2012, **16**, 2247–2270.

46 X. Wang, G. Song and T. Lou, *J. Mater. Sci. Mater. Med.*, 2010, **21**, 183–188.

47 Y. Du, X. Chen, Y. Hag Koh and B. Lei, *Mater. Lett.*, 2014, **122**, 62–65.

48 G. Ghersi, F. Carfì Pavia, G. Conoscenti, G. A. Mannella, S. Greco, S. Rigogliuso, V. La Carrubba and V. Brucato, *Chem. Eng. Trans.*, 2016, **49**, 301–306.

49 Z. Ma, C. Gao, Y. Gong and J. Shen, *Biomaterials*, 2005, **26**, 1253–1259.

50 Y. Liu, G. Dzidotor, T. T. Le, T. Vinikoor, K. Morgan, E. J. Curry, R. Das, A. McClinton, E. Eisenberg, L. N. Apuzzo, K. T. M. Tran, P. Prasad, T. J. Flanagan, S.-W. Lee, H.-M. Kan, M. T. Chorsi, K. W. H. Lo, C. T. Laurencin and T. D. Nguyen, *Sci. Transl. Med.*, 2022, **14**, eabi7282.

51 M. Polak, K. Berniak, P. K. Szewczyk, J. E. Karbowniczek, M. M. Marzec and U. Stachewicz, *Appl. Surf. Sci.*, 2023, **621**, 156835.

52 G. Ciapetti, D. Granchi, V. Devescovi, S. R. Baglio, E. Leonardi, D. Martini, M. J. Jurado, B. Olalde, I. Armentano, J. M. Kenny, F. X. Walboomers, J. I. Alava and N. Baldini, *Int. J. Mol. Sci.*, 2012, **13**, 2439–2458.

53 C. Meng, D. Tang, X. Liu, J. Meng, W. Wei, R. H. Gong and J. Li, *Int. J. Biol. Macromol.*, 2023, **235**, 123781.

54 K. Chawla, *Mater. Sci. Eng., A*, 2012, **557**, 45–53.

55 R. Akbarzadeh, J. a. Minton, C. S. Janney, T. a. Smith, P. F. James and A.-M. Yousefi, *J. Mater. Sci. Mater. Med.*, 2015, **26**(2).

56 J. K. Wise, A. L. Yarin, C. M. Megaridis and M. Cho, *Tissue Eng., Part A*, 2009, **15**, 913–921.

57 K. A. Kilian, B. Bugarija, B. T. Lahn and M. Mrksich, *Proc. Natl. Acad. Sci. U. S. A.*, 2010, **107**, 4872–4877.

58 L. Zeng, Y. Yao, D.-A. Wang and X. Chen, *Mater. Sci. Eng., C*, 2014, **34**, 168–175.

59 P. Duan, Z. Pan, L. Cao, Y. He, H. Wang, Z. Qu, J. Dong and J. Ding, *J. Biomed. Mater. Res. A*, 2014, **102**, 180–192.

60 A. Di Luca, K. Szlazak, I. Lorenzo-Moldero, C. A. Ghebes, A. Lepedda, W. Swieszkowski, C. Van Blitterswijk and L. Moroni, *Acta Biomater.*, 2016, **36**, 210–219.

61 A. Di Luca, C. Van Blitterswijk and L. Moroni, *Birth Defects Res., Part C*, 2015, **105**, 34–52.

62 M. Gelinsky, M. Eckert and F. Despang, *Int. J. Mater. Res.*, 2007, **98**, 749–755.

63 K. Atesok, M. N. Doral, J. Karlsson, K. A. Egol, L. M. Jazrawi, P. G. Coelho, A. Martinez, T. Matsumoto, B. D. Owens, M. Ochi, S. R. Hurwitz, A. Atala, F. H. Fu, H. H. Lu and S. A. Rodeo, *Knee Surg. Sports Traumatol. Arthrosc.*, 2014, **24**(7).

64 J. M. Sobral, S. G. Caridade, R. A. Sousa, J. F. Mano and R. L. Reis, *Acta Biomater.*, 2011, **7**, 1009–1018.

65 H. Lin, T. P. Lozito, P. G. Alexander, R. Gottardi and R. S. Tuan, *Mol. Pharm.*, 2014, **11**, 2203–2212.

66 T. Casalini, F. Rossi, A. Castrovinci and G. Perale, *Front. Bioeng. Biotechnol.*, 2019, **7**, 259.

67 I. W. K. Jie, K. W. A. Lee, S. E. Yoon, J. K. Song, L. K. W. Chan, C. H. Lee, E. Jeong, J.-H. Kim and K.-H. Yi, *Life*, 2025, **15**, 582.

68 E. M. Milliron, P. A. Cavendish, J. Carey, T. Barker and D. C. Flanigan, *Cartilage*, 2025, 19476035251319404.

69 S. Sonwane, S. Bonde, C. Bonde and C. Chandarana, *J. Drug Deliv. Sci. Technol.*, 2025, **107**, 106789.

70 Y. Zhang and J. Wang, *Int. J. Biol. Macromol.*, 2024, **274**, 133590.

71 H. Zhu, C. Wang, Y. Yang, H. Ma, X. Fan, Y. Zhang, Z. Dai, R. Cai and K. Qian, *Npj Flex. Electron.*, 2025, **9**, 1–11.

72 Y. Du, H. Liu, Q. Yang, S. Wang, J. Wang, J. Ma, I. Noh, A. G. Mikos and S. Zhang, *Biomaterials*, 2017, **137**, 37–48.

73 L. Fang, X. Lin, R. Xu, L. Liu, Y. Zhang, F. Tian, J. J. Li and J. Xue, *Nano-Micro Lett.*, 2024, **17**, 75.

74 W. Wei, W. Liu, H. Kang, X. Zhang, R. Yu, J. Liu, K. Huang, Y. Zhang, M. Xie, Y. Hu and H. Dai, *Adv. Healthc. Mater.*, 2023, **12**, 2300108.

75 R. Cao, Y. Xu, Y. Xu, D. D. Brand, G. Zhou, K. Xiao, H. Xia and J. T. Czernuszka, *Adv. Healthc. Mater.*, 2022, **11**, 2101643.

76 E. L. Mertz, E. Makareeva, L. S. Mirigian and S. Leikin, *JBMR Plus*, 2023, **7**, e10701.

77 F. Langenbach and J. Handschel, *Stem Cell Res. Ther.*, 2013, **4**, 117.

78 A. Pirosa, R. Gottardi, P. G. Alexander and R. S. Tuan, *Stem Cell Res. Ther.*, 2018, **9**(1).

79 Y.-R. Lou, T. C. Toh, Y. H. Tee and H. Yu, *Sci. Rep.*, 2017, **7**, 42816.

80 P. G. Alexander, R. Gottardi, H. Lin, T. P. Lozito and R. S. Tuan, *Exp. Biol. Med. Maywood NJ*, 2014, **239**, 1080–1095.

81 A. Borojević, A. Jauković, T. Kukolj, S. Mojsilović, H. Obradović, D. Trivanović, M. Živanović, Ž. Zečević, M. Simić, B. Gobeljić, D. Vujić and D. Bugarski, *Biomolecules*, 2022, **12**, 323.

82 J. Sun, J. Li, C. Li and Y. Yu, *Mol. Med. Rep.*, 2015, **12**, 4230–4237.

83 H.-H. Lee, C.-C. Chang, M.-J. Shieh, J.-P. Wang, Y.-T. Chen, T.-H. Young and S.-C. Hung, *Sci. Rep.*, 2013, **3**, 2683.

84 P. Ray and S. C. Chapman, *PLoS ONE*, 2015, **10**, e0134702.

85 S. Herberg, D. Varghai, D. S. Alt, P. N. Dang, H. Park, Y. Cheng, J.-Y. Shin, A. D. Dikina, J. D. Boerckel, M. W. Rolle and E. Alsberg, *Commun. Biol.*, 2021, **4**, 89.

86 V. Onesto, W. B. Barrell, M. Okesola, F. Amato, F. Gentile, K. J. Liu and C. Chiappini, *Biomed. Microdevices*, 2019, **21**, 44.

87 S. Ghosh, M. Laha, S. Mondal, S. Sengupta and D. L. Kaplan, *Biomaterials*, 2009, **30**, 6530–6540.

88 M. Wu, S. Wu, W. Chen and Y.-P. Li, *Cell Res.*, 2024, **34**, 101–123.